






Article

A Fast Calibration Method for Sensors of Atmospheric Detection System

Aobei Chen ^{1,2,†} , Dapeng Li ^{1,2,†} , Dezhi Zheng ^{1,2,*} , Zhongxiang Li ^{3,4,5}  and Rui Na ^{3,4,5} ¹ Research Institute for Frontier Science, Beihang University, Beijing 100191, China² School of Instrumentation and Optoelectronic Engineering, Beihang University, Beijing 100191, China³ Advanced Research Institute of Multidisciplinary Sciences, Beijing Institute of Technology, Beijing 100081, China⁴ Yangtze Delta Region Academy of Beijing Institute of Technology, Jiaxing 314000, China⁵ MIT Key Laboratory of Complex-Field Intelligent Exploration, Beijing Institute of Technology, Beijing 100081, China

* Correspondence: zhengdezhi@buaa.edu.cn

† These authors contributed equally to this work.

Abstract: To meet the needs of a large number of high-altitude meteorological detections, we need to perform fast, high-precision, and high-reliability calibrations of the sensors in the atmospheric detection system (ADS). However, using the traditional method to calibrate the sensor with high precision often takes a lot of time and increases the cost of workforce and material resources. Therefore, a method for realizing fast sensor calibration under the current system hardware conditions is required. A physical field model of Tube–Air–ADS is proposed for the first time, and the transfer function is obtained by combining the system identification, which provides the possibility for dynamic analysis of the calibration system. A Multi-Criteria Adaptive (MCA) PID controller design method is proposed, which provides a new idea for the parameter design of the controller. It controls the amplitude and switching frequency of the controller’s output signal, ensuring the safe and stable operation of the calibration system. Combined with the hardware parameters of the system, we propose the Variable Precision Steady-State Discrimination (VPSSD) method, which can further shorten the calibration time. Comparing and analyzing the current simulation results under Matlab/Simulink, the proposed MCA method, compared with other PID controller design methods, ensures the stable operation of the calibration system. At the same time, compared with the original system, the calibration time is shortened to 47.7%. Combined with the VPSSD method, the calibration time further shortens to 38.7 s.

Keywords: fast calibration; dynamic model; atmospheric detection system; PID control method

Citation: Chen, A.; Li, D.; Zheng, D.; Li, Z.; Na, R. A Fast Calibration Method for Sensors of Atmospheric Detection System. *Appl. Sci.* **2022**, *12*, 11733. <https://doi.org/10.3390/app122211733>

Academic Editor: Xinlei Chen,
Le Yang, Tong Qin, and Chun Hu

Received: 17 October 2022

Accepted: 14 November 2022

Published: 18 November 2022

Publisher’s Note: MDPI stays neutral with regard to jurisdictional claims in published maps and institutional affiliations.



Copyright: © 2022 by the authors. Licensee MDPI, Basel, Switzerland. This article is an open access article distributed under the terms and conditions of the Creative Commons Attribution (CC BY) license (<https://creativecommons.org/licenses/by/4.0/>).

1. Introduction

Conventional high-altitude atmospheric detection is a routine scientific research activity required by the World Meteorological Organization (WMO) [1,2]. It can capture the instantaneous distribution of temperature, humidity, pressure, and other meteorological parameters at any altitude, which is essential for weather analysis and forecasting [3,4]. According to statistics, more than 14,500 weather stations worldwide are expected to incorporate more than two million atmospheric detection systems (ADS) annually [5]. The high demand for atmospheric sounding requires systems to ensure the high performance of each sensor while keeping costs low [6–8]. The ADS integrates several different sensors to obtain in situ data on all aspects of atmospheric detection [9,10]. As one of the most critical sensors in system integration, the temperature sensor can not only solve the temperature information of the environment in real-time but also improve the accuracy of sensors such as pressure and humidity through temperature compensation [11–13]. The accuracy of temperature sensor measurements is crucial.

To test the performance of temperature sensors in ADS, we often place the sensor in a known environment where the temperature can be accurately measured. By testing the error of the sensor output with the known ambient temperature, the sensors' accuracy performance can be obtained [14,15]. However, ADS operates over a wide range between $-80\text{ }^{\circ}\text{C}$ to $50\text{ }^{\circ}\text{C}$ [16]. The traditional calibration instrument adopts the thermostat open-loop calibration method, which has low calibration efficiency, low safety, and high energy consumption [17,18]. It cannot meet the large-scale requirement nor the fast and high precision of ADS.

A common way to increase the speed of sensor calibration is to replace manual calibration with automated equipment [19,20]. In [21], an automatic and fast calibration method for sensors was proposed. However, this method only optimizes the calibration process and does not analyze the dynamic performance of the calibration system. In [22], an active control sampling method was proposed, which trains the system before sensor data collection. However, this method is unsuitable for situations with little prior knowledge of the sensor [23–25]. In [26], a fast dynamic calibration method was proposed, which predicts the sensor's transfer function according to the dynamic data during the calibration process and improves the efficiency of the sensor calibration process. However, this method has high requirements for the stability of the calibration system and low resistance to external interference. The above cases show that using automated procedures to calibrate the sensor can improve efficiency. However, there are still significant challenges in analyzing system dynamic performance and control strategies [27,28].

To realize the automatic control of temperature sensor calibration, we must obtain the dynamic transfer function of the temperature sensor to complete the design of the system control strategy. In [29], dynamic models of temperature sensors in benchmark tubular reactors were built, and their sensitivity to external perturbations was analyzed. In [30], a dynamic model of a bridge temperature sensor powered by dual constant current sources was developed. The sensor was calibrated, and the results showed promising results in high-temperature areas. In [31], a dynamic model of a hybrid system for measuring temperature using an optical fiber and a bimetal element was developed, and the sensor was calibrated. Existing research has established a relatively complete dynamic model of the temperature sensor. However, the system environment in which the sensor is located is different. In ADS, the dynamic model established before is no longer applicable.

In many essential projects related to people's livelihood, such as smart energy management [32], techno-economic feasibility of photovoltaic solar generation systems [33], and permanent magnet synchronous motor [34], many advanced control algorithms have been used to obtain more satisfactory results. For the calibration system, to control the cost, the control computer in the system can often only provide the classical PID control method [35,36]. The key to the success of the PID control method is how to design the parameters of the control system [37]. The Ziegler–Nichols (Z-N) tuning method in [38], which can design the controller's parameters, requires some prior knowledge and manual tuning. The Transfer-Function-Based (TFB) method in [39] can adjust the controller's parameters according to the transfer function's characteristics to obtain better performance. The Fuzzy PID method in [40] can dynamically adjust the parameters of the PID controller during the system response phase. Many excellent PID controller design methods have been proposed in the existing research. However, the control signal input to the incubator must be tightly controlled in terms of amplitude. Excessive control signals will lead to increased energy consumption or even damage the thermostat. Meanwhile, the cooling and heating of the incubator are controlled by the compressor and the resistor, respectively. The rapid switching of temperature states will cause the compressor to start and frequently stop, resulting in damage. Therefore, the switching frequency of the control signal input to the incubator must be strictly controlled. The existing PID controller design methods cannot temporarily meet the controller parameter design's needs in the calibration system.

Without a fast calibration method for temperature sensors in ADS, daily, high-altitude atmospheric detection is questionable. This paper provides a Tube–Air–ADS physics model

for the first time, which is used to obtain the system's dynamic transfer function in the temperature calibration process. According to the actual situation of the calibration system, the model combines the Navier–Stokes equation and the energy equation to establish a finite element model. Then, the system is identified by the Sanathanan–Koerner (S-K) iterative method, and the dynamic transfer function is obtained. This paper proposes a Multi-Criteria Adaptive (MCA) PID controller design method. The input control signal amplitude and switching frequency of the thermostat are comprehensively considered to ensure the service life of the thermostat. At the same time, the calibration efficiency of the temperature sensor is improved. Combined with the designed detection circuit precision, this paper also provides a Variable Precision Steady-state Discrimination (VPSSD) method, which further reduces the calibration time of the temperature sensor. In this paper, two major aims are studied: We analyze the mode of temperature transfer and the mechanism of action in ADS. We build a suitable physical model to analyze the dynamic performance of ADS and find a reasonable method to improve the calibration speed. We design an appropriate control strategy under the existing hardware conditions. Combined with the actual system performance and parameters, we comprehensively improve the calibration speed on the premise of ensuring the safety and stability of the system. Compared with existing methods, this paper mainly makes the following improvements:

- We built a Tube–Air–ADS system and thermostat physical field model, which first obtains the dynamic transfer function of atmospheric sounding system temperature sensor calibration;
- We propose an MCA PID controller design method, which shortens the calibration time to 47.7% compared with the existing method, and at the same time, ensures the safe operation of the thermostat under extreme conditions;
- We present a VPSSD method in temperature calibration, which reduces the calibration time of the MCA PID controller design method by 38.7 s.

The rest of this paper is organized as follows. System Physics Modeling is presented in Section 2. Section 3 describes the System Control Method used in this paper. The last two parts, Sections 4 and 5, are the evaluation and conclusions, respectively.

2. System Physics Modeling

2.1. Calibration System Overview

An overview of the temperature sensor calibration system for ADS is shown in Figure 1a. It is mainly composed of the thermostat, glass tube, fixed fixture, and standard thermometer. The physical photo of the temperature sensor calibration system for ADS is shown in Figure 1b.

ADS: ADS mainly consists of a variety of sensors, a signal acquisition system, a wireless communication module, and a power supply system. The thermal resistance with a negative temperature coefficient is selected as the sensitive element of the temperature sensor in the detection system. Thermistors are susceptible to a variety of factors, including circuits and the environment. At a certain temperature, it is impossible to guarantee accurate resistivity mapping. In addition, the detection system operates at an ambient temperature of $-80\text{ }^{\circ}\text{C}$ and the electronic components of the system operate at a minimum temperature of $-45\text{ }^{\circ}\text{C}$. Therefore, it is necessary to cover the external surface of the detection system with insulation foam to ensure that the system works properly at low temperatures.

Thermostat: Temperature sensors in the ADS operate between $-80\text{ }^{\circ}\text{C}$ and $50\text{ }^{\circ}\text{C}$ and require calibration tests in thermostats in refrigeration and heating modes. An ethanol bath thermostat is used as calibration equipment. It consists of an ethanol-solution tank, a temperature control system, and a blender. The ethanol tank is equipped with a temperature sensor, through which the temperature control system controls the temperature of ethanol at the set temperature. The blender continuously blends the ethanol while the thermostat is working to ensure uniformity of temperature.

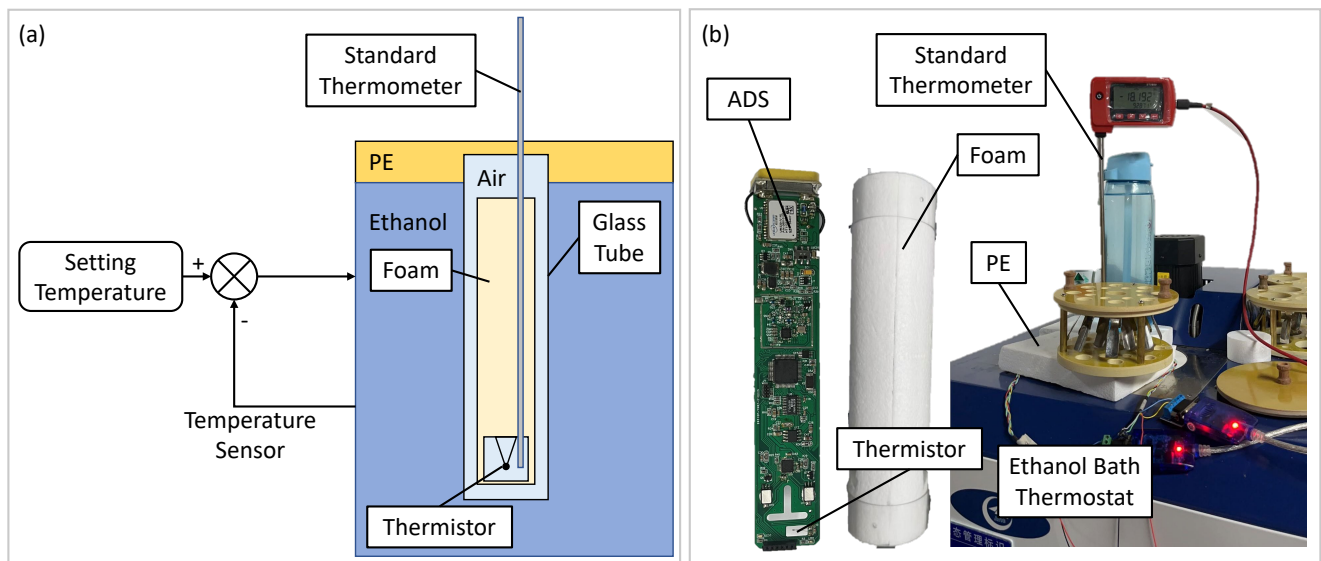


Figure 1. (a) Temperature sensor calibration system for ADS, mainly including ADS, thermostat, glass tube, fixed fixture, and standard thermometer. (b) The physical photo of the temperature sensor calibration system for ADS.

Glass tube and fixed fixture: The ADS cannot be placed directly in the thermostat ethanol solution. It needs to be placed in a glass tube for calibration. The fill gas between the sounder and the glass tube is air. The tube is fixed in an ethanol bath with a polyethylene sheet. The polyethylene sheet holds the glass tube in place and reduces the evaporation of ethanol to a certain extent.

Standard thermometer: The temperature sensor of the ethanol bath is inside the ethanol tank, and the thermal resistance of the detection system actually measures the temperature of the air in the glass tube, which cannot be guaranteed to be the same as the temperature inside the ethanol tank. The standard thermometer is placed inside the glass tube to detect the temperature near the thermistor and revise the calibration accuracy.

During calibration, a calibration point is set for each change of 10 °C. The temperature of the thermostat is set to the calibration point, and the temperature values shown by the standard thermometer are observed. When the temperature near the thermistor stabilizes, the thermistor resistance is recorded and the temperature shown in the standard thermometer. The resistance–temperature curve of the thermistor is fitted by the least squares method, and the characteristic temperature curve of the thermistor is obtained.

2.2. Dynamic Heat Transfer Model of System

To control the temperature calibration system quickly and accurately, we established a dynamic heat transfer model of the system. In the modeling process, some basic assumptions need to be put forward to ensure the simplicity and feasibility of the model and to ensure that the model can accurately restore the dynamic performance of the existing system.

2.2.1. Dynamic Heat Transfer Model of Ethanol Bath Thermostat

The heating and cooling of the ethanol bath are carried out by a heating resistor and refrigeration compressor, and the whole process is carried out at constant cooling and heating power. The compressor, heating resistor, and ethanol directly exchange heat, and the exchanged heat Q_1 can be expressed as

$$Q_1 = C_e \cdot m_e \cdot \Delta T_1, \quad (1)$$

where C_e is the specific heat capacity of ethanol, m_e is the mass of ethanol in the thermostat, and ΔT_1 is the temperature difference between the ethanol temperature and the set temperature.

Through many calibration experiments, the temperature control process of an ethanol bath thermostat is a typical first-order system. The temperature change ΔT_1 is used as the input of the thermostat. After adjusting time t_a , the system reaches a stable state with a margin of error of 2% and can be expressed as [41]

$$G_1(s) = \frac{T_1(s)}{Q_1(s)} = \frac{1}{0.25t_a \cdot s + 1} \tag{2}$$

where T_1 is the temperature of ethanol.

The temperature calibration system uses computer control, the frequency of data sampling frequency is f , and the sampling interval is $\Delta t = 1/f$, and the transfer function of the ethanol thermostat is discrete. Before the transfer function of the thermostat, the discrete transfer function is obtained by the serial Zero-Order Holder (ZOH),

$$G_1(z) = Z \left[\frac{1 - e^{-\Delta t s}}{s} G_1(s) \right] = \frac{z - 1}{z} Z \left[\frac{1}{s(0.25t_a \cdot s + 1)} \right] = \frac{1 - e^{-\frac{4\Delta t}{t_a}}}{z - e^{-\frac{4\Delta t}{t_a}}} \tag{3}$$

2.2.2. Dynamic Heat Transfer Model of Tube–Air–ADS

The structural composition of the Tube–Air–ADS is as shown in Figure 2a. The main components considered in the modeling process are air, glass tube, and foam. In order to simplify the modeling process, the geometry of the system is reduced to a two-dimensional plane rotating around the z axis, as shown in Figure 2b, and the coordinates of any point in space can be expressed in terms of height and radius. The coordinate sets of air, glass tube, and foam parts can be represented as $\Omega_{air}(z, r)$, $\Omega_{tube}(z, r)$, and $\Omega_{foam}(z, r)$, respectively. A triangular grid is used to analyze the two-dimensional area of the system, and the coordinates of the sectioning points are calculated by physical field. The results of the grid sectioning are shown in Figure 2c.

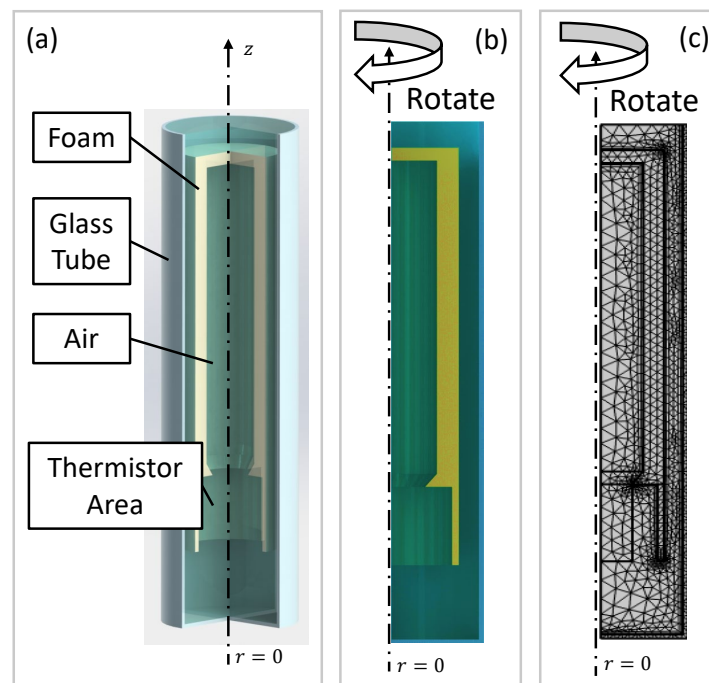


Figure 2. (a) Heat transfer model of Tube–Air–ADS structure diagram. (b) Two-dimensional structures. (c) Grid segmentation.

During the calibration of the detection system, power supply and communication with external equipment are required. The air in the glass tube flows through the holes in the polyethylene cover. The heat transfer of air in the glass tube is studied in the form

of fluid. The flow of air in the glass tube affects the heat transfer in different areas. The velocity field \mathbf{u} is updated using the Navier–Stokes equations to describe the air flow in the glass tube [42], and the velocity vector $\mathbf{u}(z, r, t)$ of the air region $\Omega_{air}(z, r)$ in the tube at any given time t ($t > 0$) can be obtained by iterating the differential equation

$$\begin{cases} \rho_{air} \left(\frac{\partial \mathbf{u}}{\partial t} + \mathbf{u} \cdot \nabla \mathbf{u} \right) = \nabla \cdot [-\rho_{air} \mathbf{I} + \mu (\nabla \mathbf{u} + \nabla \mathbf{u}^T)] + \rho_{air} \mathbf{g} + \mathbf{F} , \\ \rho_{air} \nabla \cdot \mathbf{u} = 0 \end{cases} \quad (4)$$

where ρ_{air} is air density, $\nabla \cdot$ is the dispersion operator, \mathbf{I} is unit matrix, μ is aerodynamic viscosity, \mathbf{g} is gravitational acceleration, and \mathbf{F} is the external force acting on a fluid.

Use the special forms of the energy equation mentioned in [43] to update the temperature field \mathbf{T} in the ADS. The temperature distribution of the air region in the tube at t moment is related to the solution of the velocity field $\mathbf{u}(z, r, t)$, while temperature field $\mathbf{T}(r, z, t)$ changes the velocity field distribution. The temperature field equation for air region $\Omega_{air}(z, r)$ is

$$\rho_{air} c_{p_air} \left(\frac{\partial \mathbf{T}}{\partial t} + \mathbf{u} \cdot \nabla \mathbf{T} \right) - \nabla \cdot (k_{air} \nabla \mathbf{T}) = Q_2 + Q_p + Q_{vd}, \quad (5)$$

where c_{p_air} is the constant pressure heat capacity of air, k_{air} is the thermal conductivity of air, Q_2 is the heat power transferred from the outside to the air, Q_p is the thermal power generated by the compression or expansion of the air, and Q_{vd} is viscous dissipation.

The heat transfer of the system involves two other solid materials, glass tube wall $\Omega_{tube}(z, r)$ and insulating foam $\Omega_{foam}(z, r)$ on the outside of the ADS. The temperature field equation for solid materials is

$$\rho_{tube} c_{p_tube} \left(\frac{\partial \mathbf{T}}{\partial t} + \mathbf{u} \cdot \nabla \mathbf{T} \right) - \nabla \cdot (k_{tube} \nabla \mathbf{T}) = Q_3 + Q_{ted_tube}, \quad (6)$$

$$\rho_{foam} c_{p_foam} \left(\frac{\partial \mathbf{T}}{\partial t} + \mathbf{u} \cdot \nabla \mathbf{T} \right) - \nabla \cdot (k_{foam} \nabla \mathbf{T}) = Q_4 + Q_{ted_foam}, \quad (7)$$

where ρ_{tube} is tube density, c_{p_tube} is the constant pressure heat capacity of tube, k_{tube} is the thermal conductivity of tube, Q_3 is the heat power transferred from the outside to the tube, and Q_{ted_tube} is the elastic thermal power of tube. Equation (6) describes the definition of the same parameters related to foam as Equation (7).

The heat exchange between the Tube–Air–ADS and the outside world consists of two parts. One is the heat flux A formed by the air at the tube mouth and the room environment, and the other is the inward heat flux B formed by the tube wall and the ethanol bath thermostat:

$$q_{top} = h_{top} (T_{room} - T), \quad (8)$$

$$q_{side} = h_{side} (T_{eth} - T), \quad (9)$$

where h_{top} is the heat transfer coefficient of air at the top of the glass tube, T_{room} is the indoor ambient temperature, h_{side} is the heat transfer coefficient of the side wall of the tube, and T_{eth} is the ethanol temperature.

Since there is a blender in the ethanol bath, the flow of ethanol outside the tube is calculated by forced convection. The heat transfer coefficient can be expressed by

$$h_{side} = \frac{k_{eth}}{D} \left\{ 0.3 + \frac{0.62R_e D^{1/2} P_r^{1/3}}{\left[1 + \left(\frac{0.4}{P_r} \right)^{2/3} \right]^{1/4}} \left[1 + \left(\frac{R_e D}{2.82 \times 10^5} \right)^{5/8} \right]^{4/5} \right\}, \quad (10)$$

where D is the diameter of the glass tube, R_e is the Reynolds number, P_r is the Prandtl number, and k_{eth} is the thermal conductivity of ethanol.

During the iteration of the equation, the air in the tube undergoes heat exchange with the tube inner wall, indoor environment, foam, etc., and the temperature field $\mathbf{T}(z, r, t)$ and velocity field $\mathbf{u}(z, r, t)$ are continuously updated with parameters. Finally, the temperature field and velocity field reach a stable state. Temperature T' in the thermistor region at t_i is obtained after a given temperature step $T_i (i = 1, 2, \dots, n_u)$ is entered t_i . The dynamic heat transfer function of the glass tube air-probe system can be described as $G_2(z) = M(z)/D(z)$. The number of zeros and poles of $G_2(z)$ will be determined according to the form of the system step response.

The time domain function of the system has a complex form; so, it is difficult to obtain the transfer function of the system through the Laplace transform. The system transfer function can be analyzed as the time domain waveform of the system dynamic response, which is a nonlinear least squares problem. Using the Sanathanan–Koerner (S-K) iterative method for least squares solution [44], the solution objective function can be described as

$$\underset{D, M_i}{\text{minimize}} \sum_{k=1}^{n_f} \left| W(\omega_k) \left[T'_i(\omega_k) - \sum_{i=1}^{n_u} \frac{M_i(\omega_k)}{D(\omega_k)} T_i(\omega_k) \right] \right|^2, \quad (11)$$

where ω_k are the frequency points involved in the process of solving the objective function optimally, W is the associated weight of the specified frequency, and n_k is the number of frequency points selected.

3. System Control Method

3.1. MAC PID Controller Design Method

Figure 3 shows the structure of the PID control system, where $T^*(t)$ represents the discrete temperature setting signal input, $e^*(t)$ represents the discrete control signal input to the PID controller, $c^*(t)$ represents the discrete temperature control signal output from the PID controller to the thermostat, and $T'(t)$ represents the continuous temperature change of the temperature sensor. In the process of parameter setting of the PID control method, only the steady-state time and overshoot of the final output $T'(t)$ are considered, and the controller output is ignored. This will cause the signal $c^*(t)$ output from the controller to have a larger amplitude, or to change direction too quickly, eventually leading to damage to the thermostat.

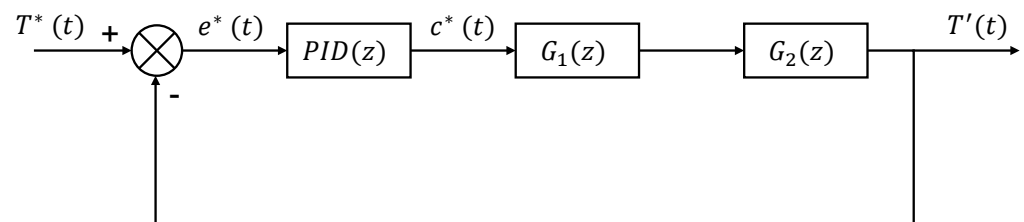


Figure 3. PID control system structure.

Based on the original PID, the input temperature limit T_s and the minimum switching time t_s of the working state are added as the main standard; the parameters are time-adjusted automatically according to the prescribed procedure; the adaptive parameter adjustment process of PID parameters is achieved; the long-term stability of the thermostat

is guaranteed; and the rapidity and stability of $T'(t)$ is also guaranteed, which improves the reliability of the system.

In the process of ethanol temperature adjustment, we limit the change of setting temperature and avoid damage to the instrument. The input temperature change limit value is T_s . The temperature setting limit criterion function can be expressed as

$$f_{limit}(t) = \begin{cases} 1 & |c^*(t) - T^*(t)| \leq T_s \\ 0 & |c^*(t) - T^*(t)| > T_s \end{cases} \quad (12)$$

Heating and cooling of the converter is completed by switching between the compressor and the heating resistor. Switching in a shorter time can cause damage to the compressor; so, it is necessary to limit the switching time of the working state. The minimum switching time of the working state is t_s . The switching time limit criterion can be expressed as

$$f_{switch}(t) = \begin{cases} 1 & \prod_{j=1}^{t_s/\Delta t} \frac{c^*[t-(j-1)\Delta t] - c^*(t-j\Delta t)}{\Delta t} \geq 0 \\ 0 & \prod_{j=1}^{t_s/\Delta t} \frac{c^*[t-(j-1)\Delta t] - c^*(t-j\Delta t)}{\Delta t} < 0 \end{cases}, t \in (t_s, +\infty). \quad (13)$$

where Δt is the sampling time of the discrete control system.

Based on the adjustment time and overshoot criterion designed by the PID controller, temperature setting criteria and switching time limit criterion were added, and adaptive adjustments were made based on the set expected performance indicator parameters, as shown in Algorithm 1.

3.2. VPSSD Method

In judging the adjustment time t_p , the stable range of the acceptable steady-state error e_{ss} needs to be given. However, due to the resistance temperature characteristics of Negative Temperature Coefficient (NTC) thermistor and the accuracy of the detection circuit, the e_{ss} steady-state error range will change in the larger temperature range. By calibrating different temperature ranges and combining with the precision of the detection circuit, the steady-state error range of the response is given, and the calibration speed is further improved.

A typical NTC thermistor detection circuit is shown in Figure 4, where R_{NTC} is the thermistor, R_1 and R_2 are voltage divider resistors, C is the filter capacitor, A_{IN} is the analog signal input of the Analog-to-Digital Converter (ADC), and REF is the reference voltage input. R_{NTC} changes with temperature during operation, resulting in a change in its input voltage to A_{IN} . The ADC compares the input voltage with the reference voltage REF to obtain the quantized resistance value, and the temperature at this point can be obtained through subsequent computer processing.

The resistance value in NTC thermistor changes with the change in external temperature, and the relationship between its resistance and temperature change can be described as

$$R_{NTC} = R_0 \exp\left\{B\left(\frac{1}{T} - \frac{1}{T_0}\right)\right\}, \quad (14)$$

where R_0 is the resistance of the thermistor at 25 °C, T is the ambient temperature, $T_0 = 298.15$ K, and B is the constant associated with the thermistor.

Algorithm 1	MAC PID Controller Design Method
Input:	Temperature setting signal $T^*(t)$, system temperature response $T'(t)$, controller output $c^*(t)$, initial parameters of the PID controller, adjustment time limit t_b , overshoot $\sigma\%$, temperature setting limit T_s , switching time limit t_s , steady-state error resistance e_{ss} , calibration points q .
Output:	Proportional coefficient P , integral coefficient I , differential coefficient D , and filter order N after adjustment of MCA PID parameters.
1:	for all $i = q, q+1, \dots, t/\Delta t$ do
2:	$band = \{T'(i-q+1), T'(i-q+2), \dots, T'(i)\}$
3:	if $100 \times T'(t) - T^*(t) T^*(t) > \sigma$
4:	Change PID controller parameters.
5:	break
6:	else if $\left\{ \frac{1}{q} \sum_{k=1}^q band(k) - T^*(t) < e_{ss} \right\} \cap \left\{ \max(band) - \min(band) \right\} = False$
7:	Change PID controller parameters.
8:	break
9:	else if $\left\{ c^*(t) - T^*(t) \leq T_s \right\} \cap \left\{ \prod_{j=1}^{t_s/\Delta t} \frac{c^*[t-(j-1)\Delta t] - c^*(t-j\Delta t)}{\Delta t} \geq 0 \right\} = Ture$
10:	return $\{P_j, I_j, D_j\}$
11:	break
12:	else
13:	Change PID controller parameters.
14:	end if
15:	end for

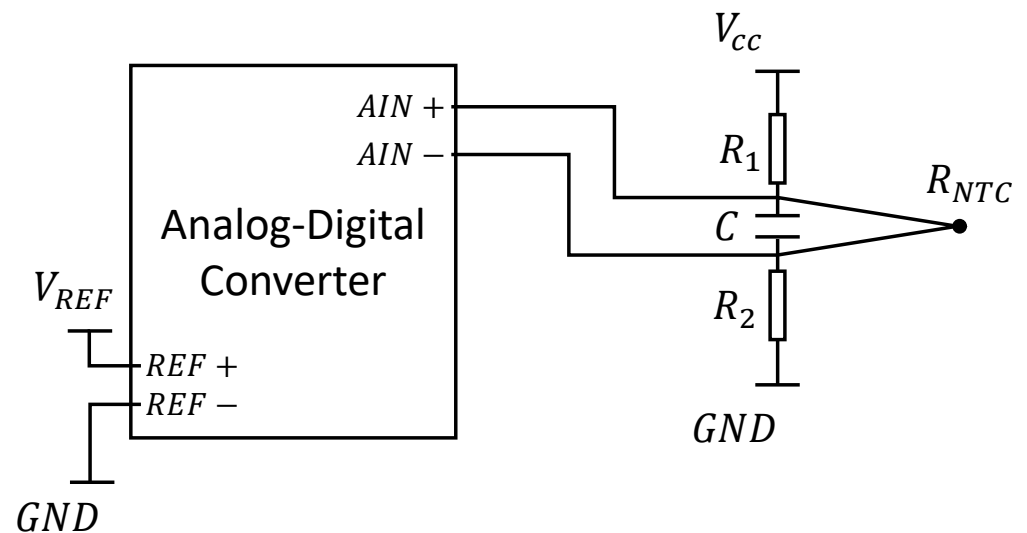


Figure 4. Thermistor temperature measurement principle.

Ideally, the resolution accuracy of the ADC voltage measurement can be expressed as $\Delta V = V_{cc}/2^p$ (p is the number of ADC bits). Combined with the NTC resistor temperature

variation law and the structure of the detection circuit, the temperature error range related to the ADC bit number p is derived as

$$\Delta T_{ADC} = \left| -\frac{\left\{ \exp \left[B \left(\frac{1}{T} - \frac{1}{T_0} \right) \right] R_0 + R_1 + R_2 \right\}^2 T^2}{2^p \exp \left[B \left(\frac{1}{T} - \frac{1}{T_0} \right) \right] R_0 (R_1 + R_2)} \right|. \tag{15}$$

During the temperature calibration of NTC thermistors, when it is determined that the temperature is stable at a certain temperature point, a certain number q of the resistance value of the thermoresistor at that temperature needs to be recorded. The temperature stability criterion at the current moment can be expressed as

$$|T^*[t - (j - 1)\Delta t] - T'[t - (j - 1)\Delta t]| \leq \max\{\Delta T_{ADC}, \Delta T_{exp}\}, j \in [1, q], \tag{16}$$

where ΔT_{exp} is the expected temperature calibration accuracy set according to actual needs. The core idea of the temperature stability criterion is to select the ΔT_{ADC} and ΔT_{exp} criteria according to the state to judge the stability of the T' . The workflow is shown in Algorithm 2.

Algorithm 2	VPSSD Method
Input:	Temperature setting signal $T^*(t)$, system temperature response $T'(t)$, temperature error range related to the ADC ΔT_{ADC} , the expected temperature calibration accuracy ΔT_{exp} , calibration points q .
Output:	Temperature stability criterion for $T'(t)$, a value of 0 is considered stable, 1 is considered unstable.
1:	$counter = 0, flag = 1$
2:	for all $i = q, q + 1, \dots, t/\Delta t$ do
2:	$counter = counter + 1$
3:	for all $j = i - q + 1, i - q + 2, \dots, i$ do
4:	if $ T^*[t - (j - 1)\Delta t] - T'[t - (j - 1)\Delta t] \leq \max\{\Delta T_{ADC}, \Delta T_{exp}\}$
5:	$flag = 0$
6:	break
7:	end if
8:	end for
9:	end for
10:	return $flag$

4. Evaluation

This section mainly focuses on the following three points to start the parameter setting and evaluation work: (1) Based on the heat transfer model of the system presented in Section 2, the transfer function of the system temperature calibration process is obtained by combining practical experiment and COMSOL finite element analysis; (2) the initial PID controller parameters are obtained by using Simulink PID Tuner toolbox combined with the actual speed and stability requirements of the system, and the control parameters are obtained by using MAC PID controller design method to compare the effectiveness of each control system; (3) combining the temperature calibration accuracy with the actual design of the hardware index of ADS, the calibration time of the system under different conditions is obtained and compared using the VPSSD method.

4.1. Dynamic Model Parameter Setting

A large number of practical experiments have proved that the ethanol temperature changes every $\Delta T_1 = 10\text{ }^\circ\text{C}$, the ethanol to achieve temperature stability of the regulation time is stable in $t_a = 120\text{ s}$, and the sampling interval is $\Delta t = 0.1\text{ s}$. Combined with Equation (3), can be obtained from the transfer function of the ethanol temperature chamber as

$$G_1(z) = \frac{3.328 \times 10^{-3}}{z - 0.997}. \tag{17}$$

In this paper, the Tube–Air–ADS system is modeled and quantified by COMSOL Multiphysics. The boundary conditions are obtained and differential equations are solved by using the laminar flow and fluid heat transfer modules. The transient processes of temperature and velocity fields in the glass tube are studied. The material parameters of glass, air, and ethanol from the COMSOL internal material library are used and the thermal conductivity $k_{foam} = 0.03\text{ W/(m}\cdot\text{K)}$, density $\rho_{foam} = 60\text{ kg/m}^3$, and constant pressure heat capacity $c_{p_foam} = 200\text{ J/(kg}\cdot\text{K)}$ of the foam are set according to the real system dimensions. Figure 5 shows the established FEA geometry model and the distribution of temperature field $\mathbf{T}(z, r, t)$ and velocity field $\mathbf{u}(z, r, t)$ at $t = 20\text{ s}$ and $t = 200\text{ s}$ after the beginning of the simulation. As the simulation progresses, the distribution of temperature and velocity fields gradually tends to the steady state.

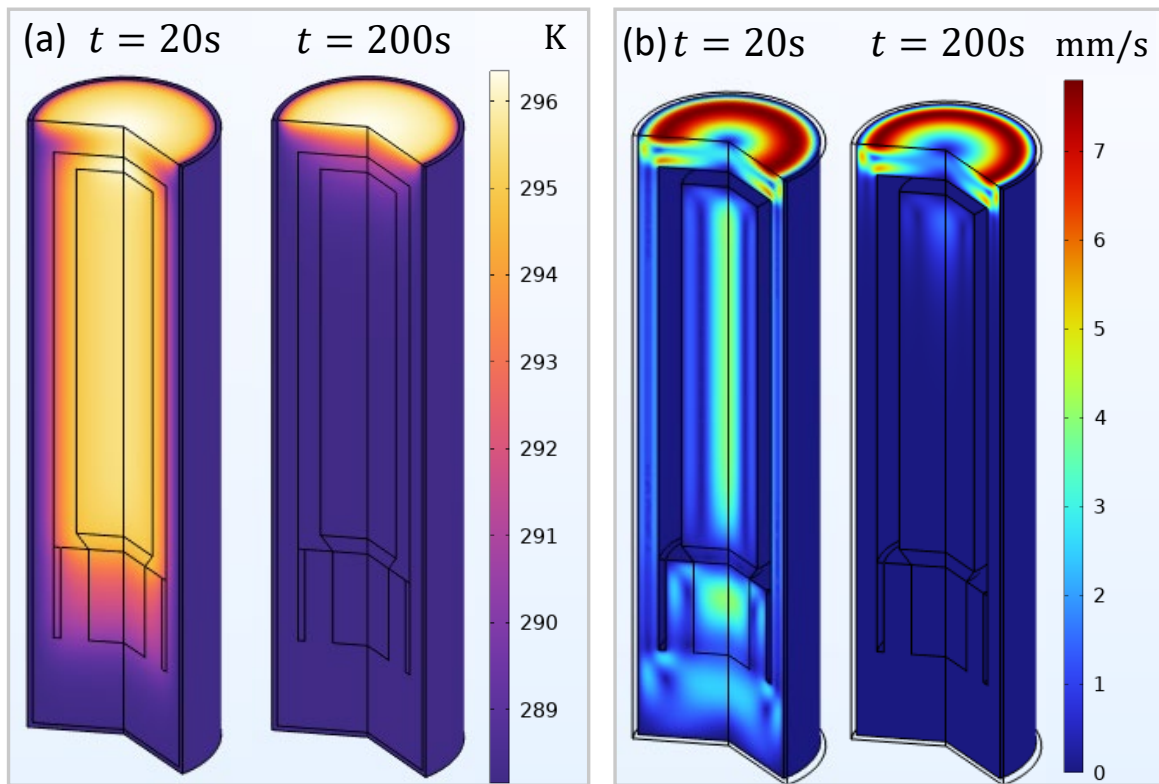


Figure 5. (a) Temperature field distribution in the glass tube at $t = 20\text{ s}$ and $t = 200\text{ s}$. (b) Velocity field distribution in the glass tube at $t = 20\text{ s}$ and $t = 200\text{ s}$.

The simulation time step Δt is set to 0.1 s and simulation time to 200 s . As shown in Figure 6, a step temperature input is given to the Tube–Air–ADS system at 10 s of the simulation, i.e., the ethanol temperature outside the glass tube is changed by $10\text{ }^\circ\text{C}$ from the steady state.

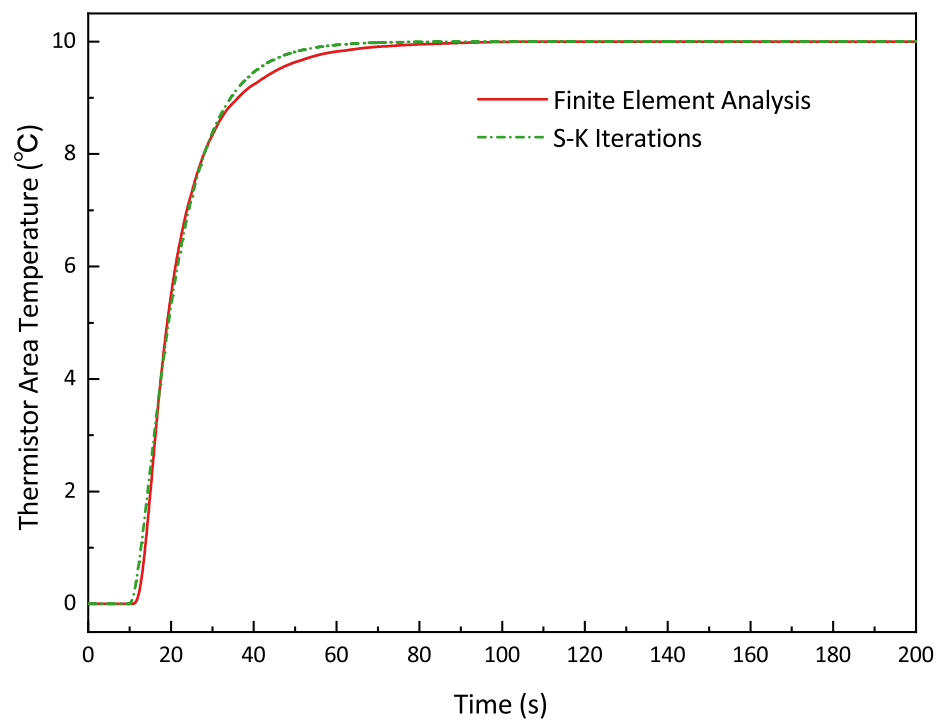


Figure 6. Finite element simulation and S-K iterative fitting of temperature dynamics.

The S-K iterative method mentioned in Equation (11) is used to fit the temperature dynamic response of the Tube–Air–ADS system obtained from the finite element analysis. $G_2(z)$ has one zero and two poles, and the sampling time $\Delta t = 0.1$ s of the system is set in the fitting process. The accuracy of the curve fit, as shown in Figure 6, is 96.29%. The dynamic transfer function of the ADS system is as follows:

$$G_2(z) = \frac{3.758 \times 10^{-4} z^{-1}}{1 - 1.955z^{-1} + 0.955z^{-2}} \quad (18)$$

4.2. Controller Parameter Setting and Evaluation

The PID parameters of the system are designed using the PID Tuner toolbox in Simulink, which is commonly used in the PID parameter tuning process, to confirm the initial optimal PID parameters of $P = 1.986$, $I = 0.069$, $D = 5.302$; then, we set the filter order $N = 0.570$ and add the designed PID controller to the loop of the temperature control system. The controller parameters are adjusted according to the MAC PID controller design method proposed in Section 3.1. The minimum adjustment time $t_s \geq 5$ s, temperature change limit $T_s \leq 15$ °C, overshoot $\sigma\% \leq 5\%$, and adjustment time $t_b \leq 150$ s are set during the adjustment process. After adjustment, the PID parameters are $P = 1.030$, $I = 0.033$, and $D = 0$.

At the same time, several mature and perfect PID controller design methods are selected for comparison [45,46]. Using the Z-N PID parameter design method [38], a set of parameters is obtained as $P = 2.383$, $I = 0.367$, and $D = 3.874$. Without human intervention, the simulation results show that this set of parameters causes the system to diverge; so, it cannot be used. Using the TFB PID parameter adjustment method in [39] and the Fuzzy PID method of automatic parameter adjustment in [40], the corresponding system response curve is obtained. The details are described below.

4.2.1. Evaluation of Adjustment Time and Overshoot Criterion

Figure 7 shows the response of the ADS temperature sensor calibration system to step control signal input with different control strategies. We set the expected temperature calibration accuracy at 0.5% steady-state error. For the step signal input, the original system

without adding the controller has no overshoot but the adjustment time is very long at 183.9 s. The PID controller is added to the original system and the adjustment time is shortened to 104.8 s; however, the system has an overshoot of 9.4%, which does not meet the requirement of overshoot $\sigma\% \leq 5\%$. Using the TFB PID parameter adjustment method, the system's dynamic performance is greatly improved and the adjustment time is only 59.2 s. However, the controller output signal of this method is not suitable for calibrating the system, which will be explained in detail later. Then, we use the Fuzzy PID control method, the overshoot of the system is 10.9%, and the adjustment time is 112.4 s. It does not obtain satisfactory stability and dynamic performance. Using the MCA PID controller design method, the overshoot of the system is only 0.7%, and the adjustment time is 87.7 s, achieving better stability and dynamic performance.

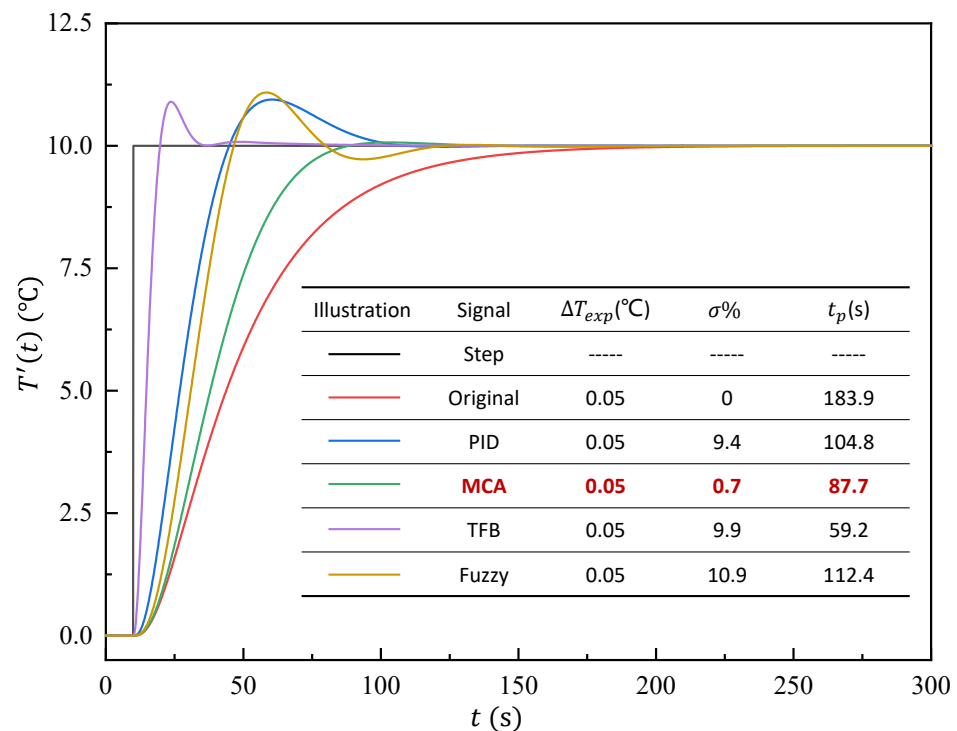


Figure 7. System response under different controllers.

4.2.2. Evaluation of Temperature Setting Limit and Switching Time Limit Criterion

Figure 8 shows the $c^*(t)$ signal output of the PID controller and the MCA PID controller. The control signal input to the temperature chamber from the PID controller outputs a maximum temperature control signal of 50.08 °C at 10 s, which exceeds the temperature change limit of $T_s \leq 15 \text{ °C}$ and does not meet the temperature setting limit criterion. For the TFB PID parameter adjustment method, there is a large mutation of the control signal. In the actual use process, it will cause direct damage to the thermostat control system. For the Fuzzy PID control method, the parameter adjustment process can be seen from the controller output signal. Its output signal is smaller than the original PID but cannot meet the system requirements. For the MCA PID controller, at 27.5 s, the output maximum temperature control signal is 13.09 °C, which meets the temperature setting standard. Combining the $c^*(t)$ signal output of the several PID controllers, it is found that the MCA PID controller design method can control the output of the control signal to the thermostat well, and can limit the output of the large value control signal to ensure the safety and stability of the thermostat process.

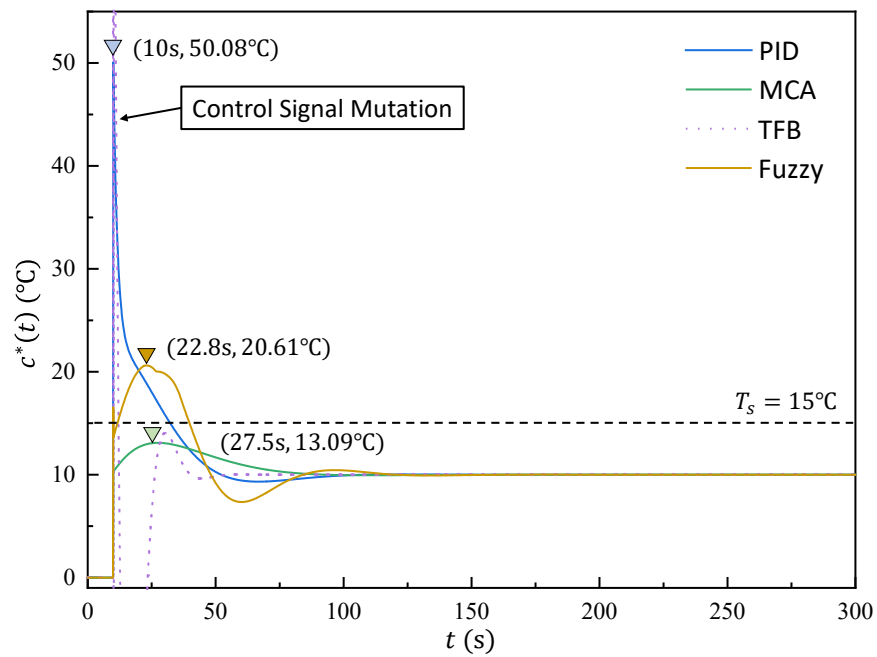


Figure 8. PID controller output signal.

Figure 9 shows the control of the working state of the thermostat by the $c^*(t)$ signal output by various controllers. The PID controller produces a heating control signal at 10.0 s and a cooling signal at 10.01 s, remaining inactive for only 0.3 s between 66.7 and 67 s, and failing to satisfy the required short adjustment time $t_s \geq 5$ s. For the TFB PID controller design method, although it has better dynamic performance in Figure 7, its control signal direction changes frequently. For the Fuzzy PID control method, the direction of the control signal frequently changes due to the automatic adjustment of the controller parameters. For the above controllers, the direction of the output signal frequently changes, which will speed up the loss of the thermostat and even cause damage to the compressor. The MCA PID control method proposed in this paper, from 106.0 s to 117.6 s, is the shortest time to maintain a working state. The time interval is 11.6 s, which satisfies the set minimum adjustment time. It can ensure the incubator’s long-term stable operation and improve the system’s reliability.

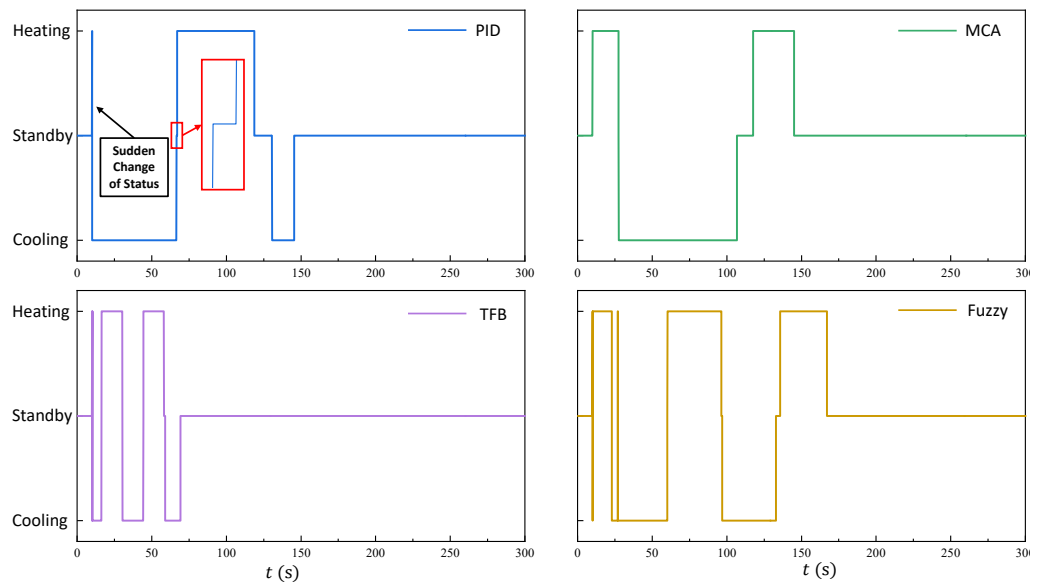


Figure 9. Ethanol thermostat working condition.

4.3. VPSSD Method and Temperature Calibration Time Evaluation

The temperature sensor used in the atmospheric detection system is a negative temperature coefficient thermistor. With glass encapsulation, the thermal conductivity is fast and the conditioning time is negligible relative to the calibration system. After a practical calibration test, the sensor resistance $R_0 = 15.60 \text{ K}\Omega$ at $25 \text{ }^\circ\text{C}$ has a B value of 3718 and the relationship between resistance change and ambient temperature can be expressed as

$$R_{NTC} = 15.60 \times \exp\left\{3718\left(\frac{1}{T} - \frac{1}{298.15}\right)\right\}. \quad (19)$$

The hardware composition of the atmospheric sounding system temperature detection circuit is the same as that shown in Figure 4. The AD7714 is used as the digital-to-analog converter chip with 24-bit detection accuracy, where $R_1 = 200 \text{ K}\Omega$, $R_2 = 100 \text{ K}\Omega$, $V_{REF} = V_{CC} = 2 \text{ V}$, and $C = 0.01 \text{ }\mu\text{F}$.

During the calibration of the thermistor, the expected temperature calibration accuracy is $\Delta T_{exp} = 0.05 \text{ }^\circ\text{C}$. Record a set of data at intervals of $10 \text{ }^\circ\text{C}$ in the $-80 \text{ }^\circ\text{C}$ to $50 \text{ }^\circ\text{C}$ temperature range. The minimum temperature variation in the external environment that the ADC detection circuit can distinguish is between $-80 \text{ }^\circ\text{C}$ and $50 \text{ }^\circ\text{C}$, as shown in Figure 10a. In the temperature range $-70 \text{ }^\circ\text{C}$ to $0 \text{ }^\circ\text{C}$, the temperature resolution accuracy of the detection circuit is higher than ΔT_{exp} . The steady-state temperature error during calibration can be set according to $\Delta T_{error} = \Delta T_{exp}$. In the temperature range $-80 \text{ }^\circ\text{C}$, $10 \text{ }^\circ\text{C}$ to $50 \text{ }^\circ\text{C}$, the temperature resolution accuracy of the detection circuit is lower than ΔT_{exp} . The steady-state temperature error during calibration can be set according to $\Delta T_{error} = \Delta T_{ADC}$.

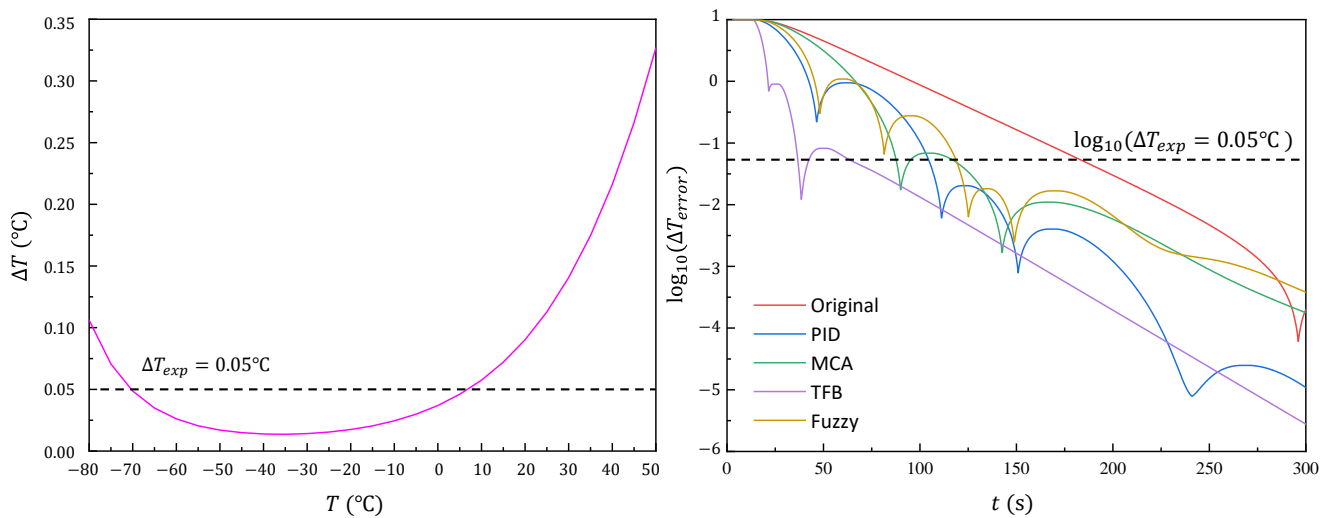


Figure 10. (a) Detection accuracy of the ADC circuit at different temperatures. (b) Stabilization time of starting calibration at different calibration temperature points.

The abscissa of the curve in Figure 10b is the calibration time, and the ordinate is the logarithmic steady-state error of the currently recorded resistance value of group $q = 30$. The ΔT_{error} corresponds to each point in the curve, the steady-state error of the first 30 points of the point is less than ΔT_{error} . The steady-state error of the current control loop at different temperature points can be found in Figure 10b by matching the final steady-state error calibration required for the current system to the coordinate point in Figure 10a. The adjustment time of each control method for different steady-state errors is shown in Table 1. Combined with the ΔT at each temperature point in Figure 10a, the ΔT corresponding to $-70 \sim 0 \text{ }^\circ\text{C}$ is the smallest; so, the steady-state time is the longest. The ΔT corresponding to $30 \text{ }^\circ\text{C}$, $40 \text{ }^\circ\text{C}$ is smaller than $50 \text{ }^\circ\text{C}$ and bigger than $-70 \sim 0 \text{ }^\circ\text{C}$; so, the steady-state time is

longer than 50 °C but less than $-70\sim 0$ °C. In general, the smaller the ΔT , the longer the steady-state time.

Table 1. Steady -state time of each control method at different temperature points.

Temperature	Original (s)	PID (s)	MCA (s)	TFB (s)	Fuzzy (s)
−80°C	163.1	99.5	84.7	35.6	80.5
−70~0°C	183.9	104.8	87.7	36.5	118.9
10°C	154.7	98.2	83.4	35.1	79.9
20°C	154.4	95.3	82.2	34.3	79.7
30°C	141.1	94.8	80.7	33.8	78.8
40°C	135.0	45.9	78.9	33.1	77.5
50°C	129.4	45.9	77.6	32.6	77.1
Total	2348.9	1318.0	1189.1	496.5	1424.7

Do not use the VPSSD method, calibrate every 10 °C in the range of $-80\sim 50$ °C according to $\Delta T_{exp} = 0.05$ °C. The adjustment time of each control method at different temperature points is shown in Table 1. For TFB and Fuzzy PID control methods, their controller signal output cannot meet the requirements. Therefore, their steady-state time has no practical application value and is no longer analyzed. The total calibration time of the original system is 2574.6 s, of the PID control method is 1467.2 s, and of the MAC PID controller design method is 1227.8 s. The total calibration time of MCA PID control is reduced to 47.7% of the original system, and the calibration time is reduced by 239.4 s on the basis of PID control while ensuring the service life of the temperature chamber.

Using the VPSSD method proposed in this paper, the total calibration time of the original system is reduced from 2574.6 s to 2348.9 s, a reduction of 225.7 s. The PID control method is reduced from 1467.2 s to 1318.0 s, a reduction of 149.2 s. The MAC PID controller design method is reduced from 1227.8 s to 1189.1 s, a reduction of 38.7 s. Therefore, for different control methods, the variable-precision steady-state discriminant method can significantly reduce the total system calibration time. Combined with the MAC PID controller design method, the total calibration time can be reduced to 46.2% of the original system. While ensuring the service life of the temperature chamber, the total calibration time is greatly improved.

5. Conclusions

For the problem of slow calibration speed of the temperature sensor in ADS, this paper proposes a fast calibration method for the sensor. The proposed MCA PID controller design method and VPSSD method optimize the established Tube–Air–ADS dynamic model’s calibration process. The goal of optimization is to maximize the calibration efficiency of the temperature sensor with the premise of ensuring the safe and stable operation of the system. This paper presents the Matlab/Simulink simulation results of the proposed controller. It is compared with the simulation results of the original system and other control strategies. The current comparative analysis results show that the proposed method effectively improves the calibration efficiency, and the total calibration time is reduced to 47.6% of the original. The maximum value of the controller output signal of the recommended method is 13.09 °C, which produces an overshoot of only 0.7%. At the same time, the minimum time interval for its signal direction change is 11.6 s. Therefore, it effectively ensures the safe and stable operation of the system. The following is a summary of the novelties and contributions of this work: We build the Tube–Air–ADS physical model, which provides the possibility to obtain the dynamic transfer function of the ADS temperature calibration process. Based on the existing system hardware, the PID controller parameter design method and VPSSD method proposed in this paper can not only improve the calibration efficiency but also ensure the safety and stability of the system. Our future work will focus on the practical and extended applications of the fast calibration method, as well as more in-depth research and experimental verification of the mechanism of the sensor calibration process itself.

Author Contributions: Conceptualization, A.C. and D.Z.; methodology and software, A.C. and D.L.; validation, A.C. and R.N.; investigation, R.N. and Z.L.; writing—original draft preparation, A.C. and D.L.; writing—review and editing, D.L.; visualization, A.C.; funding acquisition, D.Z. All authors have read and agreed to the published version of the manuscript.

Funding: This research was funded by the National Natural Science Foundation of China (Grant No. 62203056; No. 61873021; No. 61827901) and the Fundamental Research Funds for the Central Universities (Grant No. YWF-22-JC-11).

Institutional Review Board Statement: Not applicable.

Informed Consent Statement: Not applicable.

Data Availability Statement: Not applicable.

Acknowledgments: The authors thank the support and help of the Key Laboratory of Precision Opto-mechatronics Technology (Beihang University).

Conflicts of Interest: The authors declare no conflict of interest.

Abbreviations

The following abbreviations are used in this manuscript:

ADS	Atmospheric Detection System
MCA	Multi-criteria Adaptive
VPSSD	Variable Precision Steady-state Discrimination
S-K	Sanathanan–Koerner
WMO	World Meteorological Organization
PID	Proportional–Integral–Differential
Z-N	Ziegler–Nichols
TFB	Transfer Function Based
NTC	Negative Temperature Coefficient

References

1. Fu, W.; Ma, J.; Chen, P.; Chen, F. Remote sensing satellites for digital earth. In *Manual of Digital Earth*; Springer: Singapore, 2020; pp. 55–123.
2. Peterson, T.; Folland, C.; Gruza, G.; Hogg, W.; Mokssit, A.; Plummer, N. *Report on the Activities of the Working Group on Climate Change Detection and Related Rapporteurs*; Citeseer: Princeton, NJ, USA, 2001.
3. Chen, X.; Ruiz, C.; Zeng, S.; Gao, L.; Purohit, A.; Carpin, S.; Zhang, P. H-DrunkWalk: Collaborative and adaptive navigation for heterogeneous MAV swarm. *ACM Trans. Sens. Netw. (TOSN)* **2020**, *16*, 1–27. [[CrossRef](#)]
4. Chen, X.; Xu, S.; Liu, X.; Xu, X.; Noh, H.Y.; Zhang, L.; Zhang, P. Adaptive hybrid model-enabled sensing system (HMSS) for mobile fine-grained air pollution estimation. *IEEE Trans. Mob. Comput.* **2020**, *21*, 1927–1944. [[CrossRef](#)]
5. Biardeau, L.T.; Davis, L.W.; Gertler, P.; Wolfram, C. Heat exposure and global air conditioning. *Nat. Sustain.* **2020**, *3*, 25–28. [[CrossRef](#)]
6. Xu, S.; Chen, X.; Pi, X.; Joe-Wong, C.; Zhang, P.; Noh, H.Y. ilocus: Incentivizing vehicle mobility to optimize sensing distribution in crowd sensing. *IEEE Trans. Mob. Comput.* **2019**, *19*, 1831–1847. [[CrossRef](#)]
7. Lewis, A.; Peltier, W.R.; von Schneidmesser, E. Low-Cost Sensors for the Measurement of Atmospheric Composition: Overview of Topic and Future Applications. 2018. Available online: https://eprints.whiterose.ac.uk/135994/1/WMO_Low_cost_sensors_post_review_final.pdf (accessed on 23 July 2022).
8. Yu, C.; Luo, J.; Shi, R.; Liu, X.; Dang, F.; Chen, X. ST-ICM: Spatial-Temporal Inference Calibration Model for Low Cost Fine-grained Mobile Sensing. In Proceedings of the ACM MobiCom'22, Sydney, Australia, 17–21 October 2022.
9. Liu, L.; Han, Y.; Xia, Y.; Guo, Q.; Gao, W.; Guo, J. Investigation of Atmospheric Dynamic and Thermodynamic Structures of Typhoon Sinlaku (2020) from High-Resolution Dropsonde and Two-Way Rawinsonde Measurements. *Remote Sens.* **2022**, *14*, 2704. [[CrossRef](#)]
10. Bluestein, H.B.; Carr, F.H.; Goodman, S.J. Atmospheric observations of weather and climate. *Atmosphere-Ocean* **2022**, *60*, 149–187. [[CrossRef](#)]
11. Gayfulin, D.; Tsyrlunikov, M.; Uspensky, A. Assessment and adaptive correction of observations in atmospheric sounding channels of the satellite microwave radiometer MTVZA-GY. *Pure Appl. Geophys.* **2018**, *175*, 3653–3670. [[CrossRef](#)]
12. Iacovazzi, R.; Lin, L.; Sun, N.; Liu, Q. NOAA operational microwave sounding radiometer data quality monitoring and anomaly assessment using COSMIC GNSS radio-occultation soundings. *Remote Sens.* **2020**, *12*, 828. [[CrossRef](#)]

13. Iturbide-Sanchez, F.; da Silva, S.R.S.; Liu, Q.; Pryor, K.L.; Pettey, M.E.; Nalli, N.R. Toward the operational weather forecasting application of atmospheric stability products derived from NUCAPS CrIS/ATMS soundings. *IEEE Trans. Geosci. Remote Sens.* **2018**, *56*, 4522–4545. [[CrossRef](#)]
14. Chen, X.; Purohit, A.; Dominguez, C.R.; Carpin, S.; Zhang, P. Drunkwalk: Collaborative and adaptive planning for navigation of micro-aerial sensor swarms. In Proceedings of the 13th ACM Conference on Embedded Networked Sensor Systems, Seoul, Republic of Korea, 1–4 November 2015; pp. 295–308.
15. Wang, C.C.; Hou, Z.Y.; You, J.C. A high-precision CMOS temperature sensor with thermistor linear calibration in the (−5 °C, 120 °C) temperature range. *Sensors* **2018**, *18*, 2165. [[CrossRef](#)]
16. Yao, Y.; Sun, Z.; Xu, C. Applicability of Bevis formula at different height levels and global weighted mean temperature model based on near-earth atmospheric temperature. *J. Geod. Geoinf. Sci.* **2020**, *3*, 1.
17. Žužek, V.; Pušnik, I. Calibration of Air Thermometers in a Climatic Chamber and Liquid Baths. *Int. J. Thermophys.* **2017**, *38*, 1–7. [[CrossRef](#)]
18. Liu, X.; Xu, X.; Chen, X.; Mai, E.; Noh, H.Y.; Zhang, P.; Zhang, L. Individualized calibration of industrial-grade gas sensors in air quality sensing system. In Proceedings of the 15th ACM Conference on Embedded Network Sensor Systems, Delft, The Netherlands, 6–8 November 2017; pp. 1–2.
19. Nagahage, E.A.A.D.; Nagahage, I.S.P.; Fujino, T. Calibration and validation of a low-cost capacitive moisture sensor to integrate the automated soil moisture monitoring system. *Agriculture* **2019**, *9*, 141. [[CrossRef](#)]
20. Wang, P.; Yoon, S.; Wang, J.; Yu, Y. Automated reviving calibration strategy for virtual in-situ sensor calibration in building energy systems: Sensitivity coefficient optimization. *Energy Build.* **2019**, *198*, 291–304. [[CrossRef](#)]
21. Lu, M.; Zhang, N.; Liu, P.; He, J.; Zhou, Y.; Zhu, P. Automatic and rapid calibration method for temperature coefficient of fiber grating temperature sensor. *J. Phys. Conf. Ser.* **2021**, *1820*, 012141. [[CrossRef](#)]
22. Rodriguez-Lujan, I.; Fonollosa, J.; Vergara, A.; Homer, M.; Huerta, R. On the calibration of sensor arrays for pattern recognition using the minimal number of experiments. *Chemom. Intell. Lab. Syst.* **2014**, *130*, 123–134. [[CrossRef](#)]
23. Chen, X.; Wang, H.; Li, Z.; Ding, W.; Dang, F.; Wu, C.; Chen, X. DeliverSense: Efficient Delivery Drone Scheduling for Crowdsensing with Deep Reinforcement Learning. In Proceedings of the UbiComp/ISWC'22, Cambridge, UK, 11–15 September 2022.
24. Chen, X.; Xu, S.; Han, J.; Fu, H.; Pi, X.; Joe-Wong, C.; Li, Y.; Zhang, L.; Noh, H.Y.; Zhang, P. Pas: Prediction-based actuation system for city-scale ridesharing vehicular mobile crowdsensing. *IEEE Internet Things J.* **2020**, *7*, 3719–3734. [[CrossRef](#)]
25. Chen, X.; Purohit, A.; Pan, S.; Ruiz, C.; Han, J.; Sun, Z.; Mokaya, F.; Tague, P.; Zhang, P. Design experiences in minimalistic flying sensor node platform through sensorfly. *ACM Trans. Sens. Netw. (TOSN)* **2017**, *13*, 1–37. [[CrossRef](#)]
26. Yang, F.; Geng, Z.; Koneru, A.; Zhi, M.; Li, H.; Wu, N. Dynamic calibration of electrochemical sensor for accelerated analyte quantification. *IEEE Sens. J.* **2012**, *13*, 1192–1199. [[CrossRef](#)]
27. Concas, F.; Mineraud, J.; Lagerspetz, E.; Varjonen, S.; Liu, X.; Puolamäki, K.; Nurmi, P.; Tarkoma, S. Low-cost outdoor air quality monitoring and sensor calibration: A survey and critical analysis. *ACM Trans. Sens. Netw. (TOSN)* **2021**, *17*, 1–44. [[CrossRef](#)]
28. Barcelo-Ordinas, J.M.; Doudou, M.; Garcia-Vidal, J.; Badache, N. Self-calibration methods for uncontrolled environments in sensor networks: A reference survey. *Ad Hoc Netw.* **2019**, *88*, 142–159. [[CrossRef](#)]
29. Moguel-Castañeda, J.G.; Hernandez-Ayala, J.L.; Gomez-Rodriguez, R.; Bastidas-Oyanedel, J.R.; Hernandez-Martinez, E. Multi-scale Analysis to Determine the Sensitive Zones for Temperature Sensor Location in Tubular Reactors. *Chem. Eng. Technol.* **2021**, *44*, 1259–1269. [[CrossRef](#)]
30. Yang, G.; Wen, Y. A Controllable DCCS-Based PT temperature sensor in high precision molecular spectroscopy application. *IEEE Access* **2020**, *8*, 42519–42528. [[CrossRef](#)]
31. Szolga, L.A.; Mudure, F. Temperature Sensor Using a Hybrid Structure with Plastic Optical Fiber and Bimetal Element. In Proceedings of the 2021 13th International Conference on Electronics, Computers and Artificial Intelligence (ECAI), Pitesti, Romania, 1–3 July 2021; pp. 1–5.
32. Soliman, M.S.; Belkhier, Y.; Ullah, N.; Achour, A.; Alharbi, Y.M.; Al Alahmadi, A.A.; Abeida, H.; Khraisat, Y.S.H. Supervisory energy management of a hybrid battery/PV/tidal/wind sources integrated in DC-microgrid energy storage system. *Energy Rep.* **2021**, *7*, 7728–7740. [[CrossRef](#)]
33. Ullah, N.; Sami, I.; Jamal Babqi, A.; Alkhamash, H.I.; Belkhier, Y.; Althobaiti, A.; Ibeas, A. Processor in the loop verification of fault tolerant control for a three phase inverter in grid connected PV system. *Energy Sources, Part Recover. Util. Environ. Eff.* **2021**, *0*, 1–17. [[CrossRef](#)]
34. Belkhier, Y.; Achour, A.; Bures, M.; Ullah, N.; Bajaj, M.; Zawbaa, H.M.; Kamel, S. Interconnection and damping assignment passivity-based non-linear observer control for efficiency maximization of permanent magnet synchronous motor. *Energy Rep.* **2022**, *8*, 1350–1361. [[CrossRef](#)]
35. Tang, W.; Wang, L.; Gu, J.; Gu, Y. Single neural adaptive PID control for small UAV micro-turbojet engine. *Sensors* **2020**, *20*, 345. [[CrossRef](#)]
36. Al Tahtawi, A.R.; Yusuf, M. Low-cost quadrotor hardware design with PID control system as flight controller. *TELKOMNIKA (Telecommun. Comput. Electron. Control)* **2019**, *17*, 1923–1930. [[CrossRef](#)]
37. Joseph, S.B.; Dada, E.G.; Abidemi, A.; Oyewola, D.O.; Khammas, B.M. Metaheuristic algorithms for PID controller parameters tuning: Review, approaches and open problems. *Heliyon* **2022**, *8*, e09399. [[CrossRef](#)]
38. Patel, V.V. Ziegler-Nichols tuning method. *Resonance* **2020**, *25*, 1385–1397. [[CrossRef](#)]

39. Zhuo-Yun, N.; Yi-Min, Z.; Qing-Guo, W.; Rui-Juan, L.; Lei-Jun, X. Fractional-order PID controller design for time-delay systems based on modified Bode's ideal transfer function. *IEEE Access* **2020**, *8*, 103500–103510. [[CrossRef](#)]
40. Zeng, W.; Jiang, Q.; Liu, Y.; Yan, S.; Zhang, G.; Yu, T.; Xie, J. Core power control of a space nuclear reactor based on a nonlinear model and fuzzy-PID controller. *Prog. Nucl. Energy* **2021**, *132*, 103564. [[CrossRef](#)]
41. Nagrath, I. *Control Systems Engineering*; New Age International: New York, NY, USA, 2006.
42. Constantin, P.; Foias, C. *Navier-Stokes Equations*; University of Chicago Press: Chicago, IL, USA, 2020.
43. Bird, R.B. Transport phenomena. *Appl. Mech. Rev.* **2002**, *55*, R1–R4. [[CrossRef](#)]
44. Drmac, Z.; Gugercin, S.; Beattie, C. Quadrature-based vector fitting for discretized h₂ approximation. *SIAM J. Sci. Comput.* **2015**, *37*, A625–A652. [[CrossRef](#)]
45. Borase, R.P.; Maghade, D.; Sondkar, S.; Pawar, S. A review of PID control, tuning methods and applications. *Int. J. Dyn. Control* **2021**, *9*, 818–827. [[CrossRef](#)]
46. Euzébio, T.A.; Da Silva, M.T.; Yamashita, A.S. Decentralized PID controller tuning based on nonlinear optimization to minimize the disturbance effects in coupled loops. *IEEE Access* **2021**, *9*, 156857–156867. [[CrossRef](#)]